Journal of Alloys and Compounds 896 (2022) 163040

Contents lists available at ScienceDirect

Journal of Alloys and Compounds

journal homepage: www.elsevier.com/locate/jalcom

Dehydroxylation processing and lasing properties of a Nd alumino-phosphate glass

Mónica Muñoz-Quiñonero[a], Jon Azkargorta[b], Ignacio Iparraguirre[b], Rafael J. Jiménez-Riobóo[c], Gregory Tricot[d], Chongyoun Shao[e], Francisco Muñoz[a,*], Joaquín Fernández[f], Rolindes Balda[b,g]

[a] Institute of Ceramics and Glass (CSIC), Kelsen 5, 28049 Madrid, Spain
[b] Applied Physics Department, Faculty of Engineering, University of the Basque Country UPV/EHU, 48013 Bilbao, Spain
[c] Institute of Materials Science of Madrid (CSIC), Sor Juana Inés de la Cruz 3, 28049 Madrid, Spain
[d] Université Lille, CNRS UMR 8516 - LASIRE - Laboratoire Avancé de Spectroscopie pour les Interactions la Réactivité et l'Environnement, F-59000 Lille, France
[e] Key Laboratory of Materials for High Power Laser, Shanghai Institute of Optics and Fine Mechanics, Chinese Academy of Science, 201800 Shanghai, China
[f] Donostia International Physics Center (DIPC), 20018 San Sebastian, Spain
[g] Materials Physics Center CSIC-UPV/EHU, 20018 San Sebastian, Spain

ARTICLE INFO

Article history:
Received 28 September 2021
Received in revised form 22 November 2021
Accepted 28 November 2021
Available online 1 December 2021

Keywords:
Phosphate glasses
Dehydroxylation
Laser glasses
Neodymium

ABSTRACT

In this work, we have studied the preparation and properties of an alumino-phosphate glass with composition $13Na_2O$-$13K_2O$-16BaO-$4Al_2O_3$-$54P_2O_5$ (mol%). The first part of the work deals with the study of the processing conditions of the dehydroxylation of the phosphate glass, which was performed by remelting under N_2 flow using graphite crucibles. Glass samples from 5 to 50 g and Nd_2O_3 doped were submitted to dehydroxylation and the influence of temperature, time, mass of glass and viscosity were correlated with the content of water in the glasses through the coefficient of absorption of OH ions. The network structure of the glasses was also determined by means of ^{31}P and ^{27}Al 1D/2D nuclear magnetic resonance and the local environment of Nd^{3+} ions was probed by electron paramagnetic resonance. The optimized conditions of processing were then used to obtain a dehydroxylated glass with a 2.5 wt% Nd_2O_3 whose spectroscopic and laser emission properties were studied. The spectroscopic properties of Nd^{3+} ions which include, Judd-Ofelt calculation, stimulated emission cross-section of the laser transition, lifetime, and quantum efficiency are presented. Site-selective laser spectroscopy and stimulated emission obtained under selective wavelength pumping along the $^4I_{9/2}\rightarrow{}^4F_{5/2}$ absorption band were performed to determine the distribution of crystal field in which the rare earth is located, together with its influence in the pump wavelength dependence of the spontaneous and laser emissions of Nd^{3+} in this glass matrix.

1. Introduction

Phosphate glasses continue to be a subject of intense research due to the great advantages they offer for their application as rare-earth doped luminescent materials and, most particularly, as solid state lasers [1]. Industrially manufactured high energy high power laser phosphate glasses are made through a continuous melting proprietary technology, able to produce high quality optical glasses of big dimensions. At laboratory scale, however, the melting of phosphate glasses is usually done in relatively small glass batches (< 50 g) using platinum crucibles, where the melts can be moderately well conditioned, while bubbling of carrier gases can also be occasionally employed [2–4]. However, despite the many efforts done in the past regarding the dehydration of the phosphate glasses, not new methodologies have aroused that could eventually be transferred to industry. In this respect, we recently published a method of dehydroxylation based on a two-step melting procedure, by which the phosphate batch is first melted in a ceramic crucible and, then remelted in a graphite crucible at temperatures lower than the temperature of the first melting step and under a current of N_2 [5]. The glasses so obtained by this method, which can last between 5 and 10 h, have very low OH absorption coefficients and are completely free of bubbles and stria, showing very good optical homogeneity.

The main high energy high power laser phosphate glasses use Nd^{3+} ions as dopant. This ion has been recognized as one of the most efficient rare-earth ions for solid-state lasers due to its intense $^4F_{3/2}\rightarrow{}^4I_{11/2}$ emission at around 1.06 μm. To determine the suitability of a

* Corresponding author.
E-mail address: fmunoz@icv.csic.es (F. Muñoz).

https://doi.org/10.1016/j.jallcom.2021.163040
0925-8388/

Nd^{3+}-doped glass laser, a knowledge of the spectroscopic properties such as absorption and emission cross sections, peak wavelengths and linewidths, lifetimes and quantum efficiencies, and fluorescence quenching processes are required. In particular, the emission cross-section and the quantum efficiency determine the stored energy in the $^4F_{3/2}$ state and extraction characteristics [6]. Therefore, large emission cross-section and long fluorescence lifetimes are required for good laser efficiency of the $^4F_{3/2}\rightarrow{}^4I_{11/2}$ emission. Non-radiative processes, if present, reduce the lifetime which leads to a reduction of the stored energy and affect the output laser energy. These non-radiative processes include Nd-Nd concentration quenching, multi-phonon relaxation, and quenching induced by impurities such as OH groups among others. As energy transfer to OH vibrational modes is an important source of non-radiative losses in these Nd-doped glasses, dehydroxylation of the phosphate glasses is of paramount importance to achieve a good laser performance.

In this work, an alumino-phosphate glass composition was selected to carry out a study on the influence of the processing parameters over the dehydroxylation of the glasses, i.e. temperature and time of remelting under N_2, viscosity and mass of glass. The glass composition, $13Na_2O$-$13K_2O$-$16BaO$-$4Al_2O_3$-$54P_2O_5$ (mol%), is close to the available commercial phosphate laser glasses for high power lasers such as LG-750, LG770, LHG-8 [6]. As it is well known, the addition of Al_2O_3 improves the thermal and mechanical properties and chemical durability of phosphate glasses, however its content should be kept as low as possible since it decreases the stimulated emission-cross section [7,8]. On the other hand, K_2O, BaO and Na_2O improve the physical properties with little effect on the laser properties [6,9].

The main objective in this work, was to optimize the dehydroxylation process of the chosen phosphate glass in order to prepare a doped Nd_2O_3 composition with the best optical characteristics to study the spectroscopic and laser emission properties. The structure of the glass systems has also been determined by means of Nuclear Magnetic Resonance and Electron Paramagnetic Resonance spectroscopies, from which the obtained data have been related to both spontaneous and stimulated emission properties of the Nd^{3+} ions in the glasses. The optical study includes Judd-Ofelt calculation, stimulated emission cross-section of the laser transition, lifetime and quantum efficiency, and site-selective spectroscopy, to determine the distribution of crystal field in which the rare earth is located, together with its influence in the pump wavelength dependence of the spontaneous and laser emissions of Nd^{3+} in this glass matrix.

2. Experimental

2.1. Synthesis and dehydroxylation processing of glasses

The Nd-doped glasses with nominal composition $13Na_2O$-$13K_2O$-$16BaO$-$4Al_2O_3$-$54P_2O_5$ (mol%) were obtained by melting and quenching 80 g glass batches prepared by mixing raw materials $(NH_4)H_2PO_4$ (ACROS Organics, 99+%), Na_2CO_3 (Alfa Aesar, 99.5% min.) K_2CO_3 (Sigma Aldrich, ≥ 99%) Al_2O_3 (Alfa Aesar, 99.9%), $BaCO_3$ (Alfa Aesar, 99–101%) and Nd_2O_3 (Alfa Aesar, 99.99%). All batches were melted in porcelain crucibles at 1000 °C for 1 h, poured on brass plates, then pieces of masses indicated below were afterward submitted to dehydroxylation treatments following the similar scheme as the one described in reference [5], which consists on remelting the glasses in graphite boats within a horizontal mullite tube furnace under a constant N_2 flow. The study on the processing of dehydroxylation conditions was performed in samples with an 0.5 wt% Nd_2O_3 added to the nominal glass composition. In a first part, small pieces of 5 g of the as-melted glasses were submitted to dehydroxylation treatments at temperatures within the 700 °C to 850 °C range and time lengths between 1 and 5 h. Then, it was continued with the processing of samples as a function of the mass of glass (5, 10, 25 and 50 g) used in the dehydroxylation treatment for a constant temperature of 850 °C and 3 h duration, and concluded with the effect of remelting time between 3 and 10 h at 850 °C for 50 g glasses. The 50 g glasses were dehydroxylated using a graphite boat of higher dimensions, 12 × 4.5 × 2 cm^3. A final 80 g glass batch was prepared with a 2.5 wt% content of Nd_2O_3, from which 25 g were submitted to a dehydroxylation treatment at 850 °C for 10 h so as to have an optimized glass and studying its spectroscopic and lasing properties. The last were performed using a mirror-like polished sample of about 1 cm^2 and 5 mm thick.

2.2. Characterization of glasses

The composition of the glasses was checked out by means of X-ray Fluorescence Spectroscopy in a PANalytical MagicX 2400 spectrometer using the pearl method by mixing 0.3 g of glass with 5.5 g of $Li_2B_4O_7$.

Absorption coefficient of OH ions (α_{OH}) was determined by Fourier-Transformed Infrared Spectroscopy (FTIR) from spectra registered between 450 and 5000 cm^{-1} in a Perkin-Elmer Spectrum 100 spectrometer using plane-parallel, mirror-like polished glass samples between 1 and 2 mm thick. The α_{OH} was obtained as detailed in reference [5] from the absorption at 3000 cm^{-1}, using the relation $-\log(T_{3000}/T_{5000})/t$, where t is the sample thickness.

The density was determined by the Archimedes method using distilled water as immersion liquid, and molar volume has been calculated from the ratio between the molar mass of the glass nominal composition and its density.

The glass transition temperature was determined from dilation curves in a Netzsch Gerätebau model 420 PC/1 dilatometer with a heating rate of 5 K min^{-1} in air and using an Al_2O_3 standard for calibration.

High temperature viscosity measurements were performed by the rotation method in a high-temperature Haake viscometer of the cylindrical Searle type (*Haake, Karlsruhe, Germany*) equipped with a ME 1700 sensor according to the International Standard ISO 7884–2, using rotation speeds of 3–15 rpm for 15 min measurements. Three measurements were carried out at three different rotation speeds for each temperature and the viscosity (η) was calculated from the shear stress (τ) and the shear rate (γ) applied by the viscous fluid according to $\eta = \tau\gamma$ (dPa s).

Young's modulus, Poisson's coefficient and refractive index were determined through high Resolution Brillouin Spectroscopy (HRBS), using plane-parallel, mirror-like polished glass samples. The experimental setup was already described in reference [10], in which 90A and Backscattering (180) geometries were simultaneously used for which sound velocity (v) is the important physical magnitude obtained from the combination of the Brillouin frequency shift, f, and the corresponding acoustic wave vector of the scattering geometries (λ_0 is the laser wavelength), as given by:

$$v^{90A} = \frac{f^{90A}\lambda_0}{\sqrt{2}}; v^{180} = \frac{f^{180}\lambda_0}{2n} \quad (1)$$

The refractive index (at the laser wavelength of 532 nm) can be obtained using the equation below:

$$n = \frac{f^{180}}{f^{90A}\sqrt{2}} \quad (2)$$

The elastic properties of elastically isotropic solids are defined by two independent elastic constants c_{11} and c_{44}, related via the mass density to the longitudinal (v_L) and transverse (v_T) sound propagation velocities, respectively:

$$c_{11,44} = \rho\, v_{L,T}^2 \quad (3)$$

Thus, the corresponding Young's modulus (E) and Poisson's coefficient (ν) can be calculated from c_{11} and c_{44} [11]:

$$E = \rho v_T^2 \frac{(3v_L^2 - 4v_T^2)}{(v_L^2 - v_T^2)}; \nu = \frac{(v_L^2 - 2v_T^2)}{(2v_L^2 - 2v_T^2)} \quad (4)$$

Vickers hardness was calculated from the size of the indents made in a universal indentation and scratch tester model APEX-1 from CETR instruments using 100 mN loads for 10 s

In order to detect the local coordination environment of Nd^{3+} ions, the four-pulsed (π/2–τ–π/2–T1–π–T2–π/2–τ-echo) two-dimensional hyperfine sublevel correlation (2D-HYSCORE) electron paramagnetic resonance (EPR) was performed at temperature of 4 K under an external magnetic field of 350 mT. The π/2 and π pulse lengths were 16 and 32 ns, respectively. The initial values of T_1 and T_2 are both 200 ns. In order to avoid the blind spot effect, the τ value (136 ns) has been optimized by performing three pulsed electron spin echo envelope modulation (3P-ESEEM).

The ^{27}Al and ^{31}P magic angle spinning nuclear magnetic resonance (MAS NMR) experiments were performed at 104.25 and 161.96 MHz on a 9.4 T Bruker spectrometer with a 3.2-mm measurement probe operating at a spinning frequency of 20 kHz. The ^{27}Al (and ^{31}P) NMR spectra were recorded with π/12 (π/4) flip angles, 0.5 s (120 s) recycle delays and 512 (16) transients. The 2D $^{27}Al/^{31}P$ correlation map was recorded with the scalar heteronuclear multiple quantum correlation NMR sequence [12] under rotor-synchronized conditions with 2048 transients, an optimized echo delay of 9 ms and 2048 × 60 acquisition points. The chemical shifts were referred at 0 ppm to 1 M $Al(NO_3)_3$ and 85% H_3PO_4 solutions.

2.3. Spectroscopic characterization

Conventional absorption spectra were performed with a Cary 5000 spectrophotometer. Site-selective emission and excitation spectra were recorded by using as exciting light the medium wave tuning range (765–920 nm) of a continuous wave (cw) Ti:sapphire ring laser (0.4 cm^{-1} linewidth). The fluorescence from the sample was collected and dispersed by a 0.25 m monochromator, and the signal detected by an extended IR Hamamatsu H10330A-75 photomultiplier. The photomultiplier signal was processed by a lock-in amplifier. A continuous flow cryostat was used to perform the low-temperature (4.2 K) measurements.

The decay times were obtained by exciting the sample with a Ti-sapphire laser pumped by a pulsed, frequency double Nd-YAG laser (10 ns pulse width) and detecting the emission by an extended IR Hamamatsu H10330A-75 photomultiplier. The photomultiplier signal was recorded by using a Tektronix oscilloscope.

3. Results and discussion

3.1. Effect of processing conditions on the dehydroxylation of glasses

Fig. 1 shows the values of the OH absorption coefficient of samples obtained after dehydroxylation treatments on 5 g of as-melted glasses, at temperatures from 700 °C to 850 °C and time lengths of 1, 2, 3 and 5 h. For any constant time, the OH coefficient follows a decreasing trend with the remelting temperature while the values are smaller for longer times; however, it can be seen that the rate of decreasing with temperature is also smaller for higher time lengths.

The chemical composition before and after the dehydroxylation treatments has been checked out by X-ray fluorescence spectroscopy analysis of some selected glasses. Table 1 gathers the analyzed contents of the oxide components of three different as-melted phosphate glasses (G1, G2 and G3) and four samples after dehydroxylation treatments between 700 °C and 850 °C for 5 h. The average content of the oxides from the two groups of glasses, as-melted and dehydroxylated, is also shown together with the standard deviation from the average value. It can be noted that a small loss of Na_2O is systematically obtained in the as-melted glasses, but the rest of components being near the nominal composition within the limits of error. The contents of the oxides analyzed in the dehydroxylated glasses are very similar to the ones in the as-melted parent glasses, without noticing any other significant variation with respect to the nominal composition of the phosphate system.

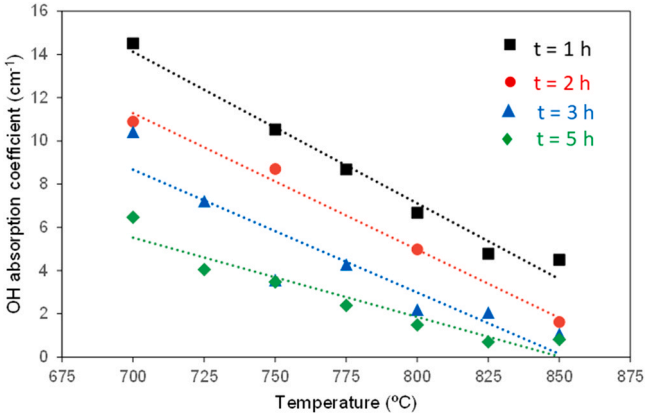

Fig. 1. OH absorption coefficients of glasses obtained by dehydroxylation at temperatures from 700 °C to for time lengths of 1, 2, 3 and 5 h. The lines represent the linear fits of the data points.

Table 1
Analyzed compositions of selected 0.2 mol% Nd_2O_3 doped glass batches and 5 g dehydroxylated glass samples after selected treatments.

Glasses	Composition (mol%)					
	Na_2O	K_2O	BaO	Al_2O_3	Nd_2O_3	P_2O_5
G1	11.16	13.46	15.78	4.34	0.23	55.03
G2	10.04	12.86	14.71	3.92	0.17	58.29
G3	11.65	13.76	15.50	4.37	0.19	54.53
Average	10.95	13.36	15.33	4.21	0.20	55.95
SD	0.82	0.46	0.56	0.25	0.03	2.04
G2-700-5	11.54	13.26	15.54	4.04	0.21	55.41
G2-800-5	12.34	13.06	15.63	4.56	0.25	54.15
G3-750-5	11.32	12.17	14.20	3.85	0.17	58.29
G3-850-5	11.44	12.22	14.10	3.83	0.18	58.23
Average	11.66	12.68	14.87	4.07	0.20	56.52
SD	0.46	0.56	0.83	0.34	0.04	2.07

As it was shown in our previous work [5], the dehydroxylation process is thermally activated and diffusion controlled throughout the release of water out from the melts, and so the OH coefficient will be inversely proportional to the melting temperature. However, the effectiveness of dehydration showed to be much higher for the first hours of remelting under N_2, showing a decrease of the OH coefficient more drastic in the first stages of the reaction and at a slower rate for longer times at each constant temperature. Furthermore, the decrease of the OH in the first hours of reaction is much higher for higher temperatures, meaning that the rate of decrease of OH with time becomes slower with the progress of the dehydroxylation reaction. Therefore, the slope of the OH vs. T plots will decrease for increasing reaction times as shown in Fig. 1.

The diffusion of water within the melts will be determined by their viscosity, so a lower melt viscosity at higher temperatures will increase the coefficient of diffusion of the water molecules, contributing to a faster dehydroxylation of the melt. Viscosity should thus be considered a key factor that will determine the dehydroxylation reaction of the glasses. Fig. 2 gathers the high temperature viscosity data of an as-melted glass batch where points have been

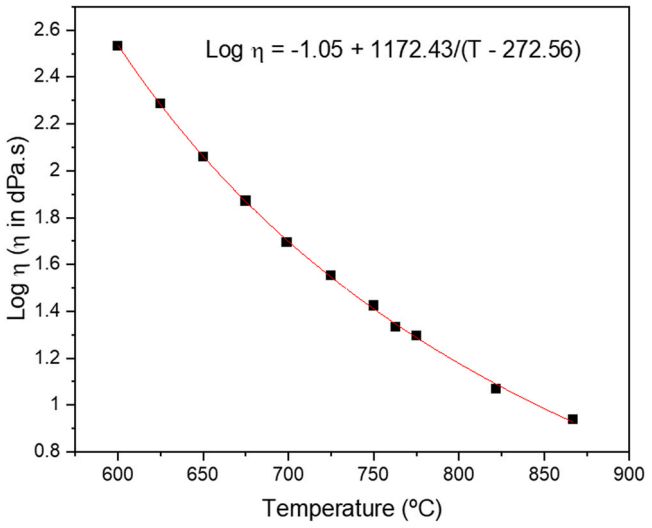

Fig. 2. Viscosity data measured by rotation and VFT fitting curve of an as-melted glass.

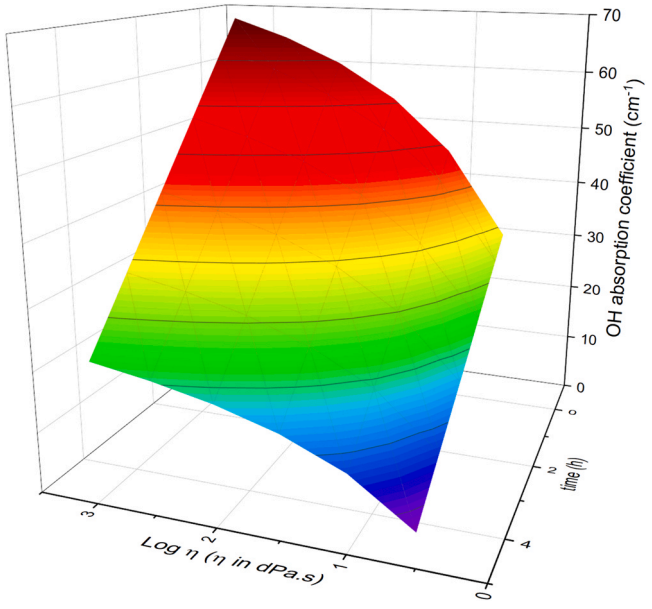

Fig. 3. 3D plot of the OH absorption coefficient against both dehydroxylation time and phosphate melt viscosity. The last has been represented from high to low values to account for the decrease of viscosity for increasing treatment temperatures.

fitted to the Vogel-Fulcher-Tammann (VFT) equation and which result is shown inside the graph.

Within the temperature and time ranges studied, the absorption coefficient of water in the dehydroxylated glasses has been fitted to linear equations as a function of temperature. Furthermore, the values of the slope and intercept of the OH coefficient vs temperature plots have also been fitted to linear equations depending on time. If one now substitutes the variable of temperature from the VFT equation of viscosity, it is possible to calculate the OH coefficient as a function of both viscosity and time. Fig. 3 shows a 3D plot of the calculated OH coefficient for viscosities between 3 and 0.5 h, in Log η units, and times up to 5 h.

The diffusion of water throughout the melts can be analyzed by means of the Stokes-Einstein relationship by which the diffusion coefficient of a particle through a fluid can be obtained from Eq. (5):

$$D = k_b T/6\pi\eta r \quad (5)$$

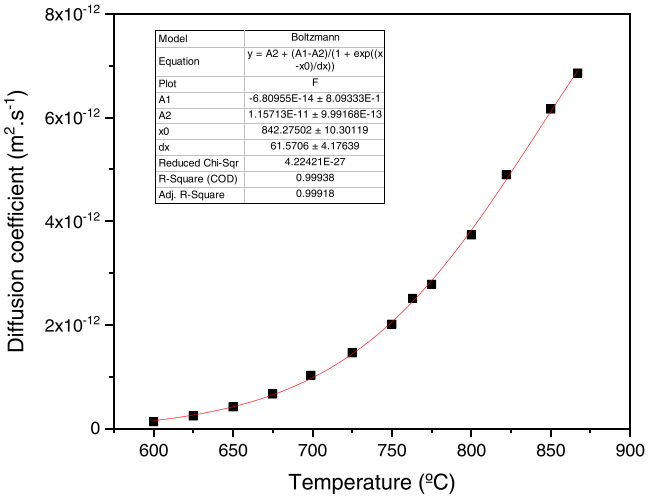

Fig. 4. Diffusion coefficient of water molecules calculated from equation of Stokes-Einstein as a function of melt temperature between 600 °C and 850 °C.

where k_b is the Boltzmann constant, T the absolute temperature, η the viscosity and r the radius of the diffusing particle, which for H_2O has been taken as $1.4{\cdot}10^{-10}$ m. Fig. 4 plots the diffusion coefficient calculated using Eq. (5) and the viscosity in Fig. 2 for temperatures between 600 °C and 875 °C. The points have been fitted to a Boltzmann growth function of the type of Eq. (6) and indicated in the inset of the figure.

$$y = (A_1\text{-}A_2)/(1+e^{(x-x0)/dx}) + A_2 \quad (6)$$

where A_1 and A_2 are adjustable parameters and x_0 represents the center at which y takes the value of $(A_1 + A_2)/2$. The x_0 after fitting is 842°C that could be supposed to be a temperature value at which the rate of increase of diffusion coefficient would be the highest. At higher values of temperature, the diffusion coefficient will experience a reduction of its increasing rate, that goes parallel to the smaller decreasing rate of viscosity with temperature, until reaching the upper limit at $y = A_2$. Therefore, 850 °C could be taken as a temperature of maximum rate of dehydroxylation given the viscosity of this melt. The diffusion coefficient calculated at T = 850 °C is $6.16{\cdot}10^{-12}$ m^2 s^{-1}, which is of a similar order than the one measured in LG-770 and LHG-8 phosphate laser glasses at temperature somehow bigger [13].

The effect of the mass of glass used in the dehydroxylation has also been studied and the results are plotted in Fig. 5, where the OH absorption coefficient has been represented against the mass of as-

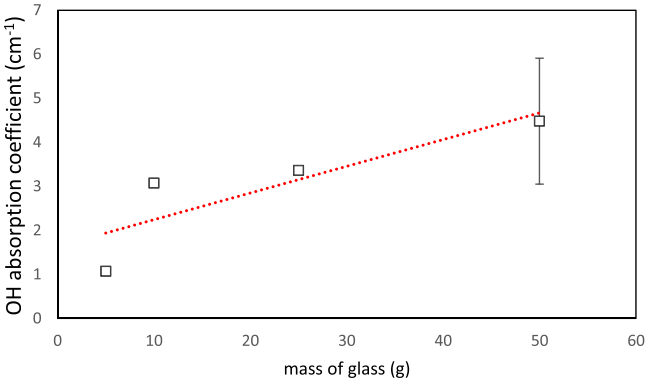

Fig. 5. OH absorption coefficient of dehydroxylated glasses against the mass of the glass submitted to treatment, for 5, 10, 25 and 50 g. Data for 50 g glass represent the average from three parts of the glass and error bar means standard deviation from average. Line represents linear fitting curve to data points.

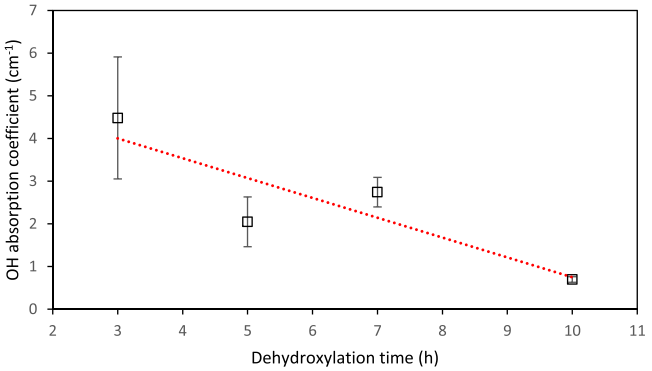

Fig. 6. OH absorption coefficient of 50 g dehydroxylated glasses against treatment time for 3, 5, 7 and 10 h time lengths. Data points are calculated from the average of three parts of the glasses, right, left and center, and error bars mean standard deviation from average. Dotted line represents a linear fit of the points.

melted glasses for 5, 10, 25 and 50 g, at 850 °C for 3 h. The absorption coefficient in the 50 g glass sample was measured in three different parts, right- and left-hand sides and center part of the glass, from which the average value and standard deviation are shown in the Fig. 5. The OH absorption coefficient increases with the mass of glass from about 1 cm^{-1} in the 5 g sample to ca. 4.5 cm^{-1} in the 50 g. Considering that the OH coefficient changes linearly with the mass of glass, as represented by the dotted line on the figure, it would increase at a rate of about, or below, 0.1 cm^{-1} per g of glass. It is worth noticing that the error in the determination of the OH coefficient in the 50 g sample, by measuring it in three different parts of the glass, may appear quite big and be representative of a low homogeneity regarding the water content. It is assumed that the error would be smaller with the decrease of the size of the dehydroxylated samples; however, in order to look for glasses with higher homogeneity, several glasses of 50 g each have been submitted to dehydroxylation for increasing times. Fig. 6 shows the OH absorption coefficient for reaction times of 3, 5, 7 and 10 h, at 850 °C, where data points correspond to the average of the coefficient measurements in the same three parts of the glasses and the error bar the standard deviation from the average. Again, one may see that the decrease of the OH coefficient is linear with the dehydroxylation time as in Fig. 1. However and most importantly here, the deviation from the average represented by the error bars becomes smaller with the increase of reaction time, being as small as the size of the symbol for the 10 h dehydroxylated glass. This means that longer reaction times will contribute to obtain glasses with a very high homogeneity.

The homogeneity of the dehydroxylated glasses was also tested through Brillouin spectroscopy and indentation measurements. Table 2 gathers the density, Young's modulus, refractive index, coefficient of Poisson and Vickers hardness from measurements in three parts of the dehydroxylated glasses at 850 °C for 3 and 10 h, as it was done with the OH coefficient in Fig. 6. Each of the two groups of samples belong to a different batch of as-melted glasses (G4 and G5 glass batches) and therefore, the values of properties would depend in first place of their analyzed chemical composition. The two glasses before dehydroxylation were analyzed by XRF spectroscopy and it was found a difference in the Al_2O_3 content, being of 4.6 wt% in the G4 glass and 3.23 wt% in the G5, which would be the reason for the higher E and H_v values of G4 glasses dehydroxylated for 3 h. The values of properties in Table 2 have been averaged in the two group of samples and results of standard deviation with respect to the average demonstrate that the properties of the 10 h samples are much closer to each other than in the 3 h group, showing again that the homogeneity of the glasses increases with the increase of the dehydroxylation time similarly to the OH content. Furthermore, dilatometry measurements revealed that the glass transition temperature of the three samples in the G4 glass, obtained by dehydroxylation at 850 °C for 3 h, were the same, 382 °C, 383 °C and 383 °C, within 0.5 °C difference.

The network structure of the G4-850-3 glass was studied by NMR and is described below. As expected from the low Al_2O_3 content, Al atoms are present as [6] Al units, as indicated by the signal observed at ca. − 20 ppm in the ^{27}Al MAS NMR spectrum (Fig. 7a-ii) [7]. The 2D $^{27}Al(^{31}P)$ J-HMQC map (Fig. 7a-i) clearly shows a correlation signal involving [6]Al and P atoms, indicating thus the presence of P-O-Al bonds in the glass network. The ^{31}P 2D maps projection (Fig. 7a-iv), that reveals the P attached to Al atoms, can be decomposed in two components assigned to Q^2_{1Al} and Q^2_{2Al}, i.e. to P atoms attached to two other P atoms and to 1 and 2 hexa-coordinated Al atoms. This decomposition was then used as input parameters for the decomposition of the 1D ^{31}P MAS NMR spectra [14,15] as reported in Fig. 7b. It turns out that the glass contains 4 different species including pure Q^2 and Q^1 as well as the previously mentioned Q^2_{1Al} and Q^2_{2Al} units. Fig. 7b also shows that the signal lying around − 30 ppm is not related to pure Q^3 but to mixed species. In our system, introduction of Al_2O_3 in the formulation produces the formation of mixed alumino-phosphate species but does not promote Q^2 disproportionation unlike what was recently observed in the zinc metaphosphate system [16].

The 2D-HYSCORE EPR spectra were obtained in an as-melted glass and a dehydroxylated one after remelting at 850 °C for 5 h, shown in Fig. 8a and b, respectively. At the external magnetic field of 350 mT, two diagonal signals located at 3.88 and 6.0 MHz correspond to the Larmor frequencies of ^{27}Al and ^{31}P nuclei, respectively. The signal intensity of ^{31}P is much stronger than that of ^{27}Al, and the extension of ^{31}P signal in the direction perpendicular to the diagonal is greater than that of ^{27}Al. This result indicates that the hyperfine interaction between ^{31}P and the unpaired electrons of Nd^{3+} ions is stronger than that between ^{27}Al and that of Nd^{3+} ions. Since the length of the chemical bond is about 2 Å, the detection distance of HYSCORE is between 4 and 8 Å. Therefore, it can be inferred that ^{31}P may be mainly located in the second coordination sphere of Nd^{3+} ions, and ^{27}Al may be located in the third or even higher coordination sphere of Nd^{3+} ions. The magnetic nuclei ^{17}O, which is expected to be located in the nearest neighbor environment of the Nd^{3+} ions,

Table 2
Density, Young's modulus, refractive index, coefficient of Poisson (ν) and Vickers hardness of two groups of samples taken at the right (-r), left (-l) and center (-c) parts of the 50 g glasses obtained by dihydroxylation treatments at 850 °C for 3 (G4 glasses) and 10 h (G5 glasses).

Sample	D (g/cm^3)	E (GPa)	n^{532}	ν	Hv (GPa)
G4-850-3-r	2.8357	49.9 ± 0.3	1.5011 ± 0.0046	0.27 ± 0.002	4.7 ± 0.1
G4-850-3-c	2.8227	50.09 ± 0.48	1.5005 ± 0.001	0.269 ± 0.004	4.3 ± 0.1
G4-850-3-l	2.8630	51 ± 0.4	1.4945 ± 0.0023	0.27 ± 0.003	3.9 ± 0.1
Average ± SD	2.84 ± 0.02	50.4 ± 0.95	1.4987 ± 0.0036	0.27 ± 0.001	4.3 ± 0.4
G5-850-10-r	2.8374	46.27 ± 0.4	1.4914 ± 0.002	0.275 ± 0.004	3.9 ± 0.1
G5-850-10-c	2.8334	46.5 ± 0.36	1.4850 ± 0.002	0.274 ± 0.003	4.1 ± 0.1
G5-850-10-l	2.8178	46.18 ± 0.44	1.4883 ± 0.0043	0.276 ± 0.003	3.7 ± 0.1
Average ± SD	2.83 ± 0.01	46.3 ± 0.17	1.4882 ± 0.0032	0.275 ± 0.001	3.9 ± 0.2

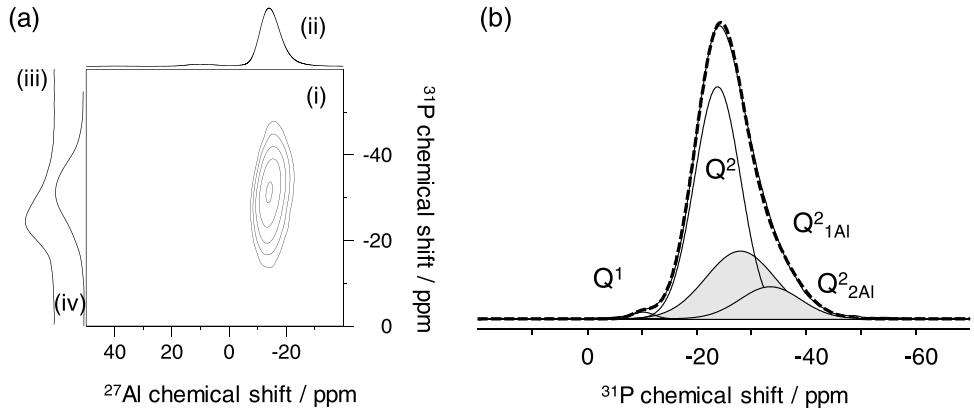

Fig. 7. (a) 2D ^{27}Al/^{31}P correlation map obtained on the G4-850-3 glass. The 2D map (i) is accompanied by the 1D ^{27}Al (ii) and ^{31}P (iii) MAS NMR spectra and by the ^{31}P 2D map projection showing the P attached to Al atoms (iv); (b) 1D ^{31}P MAS NMR decomposition using the data retrieved from the 2D maps.

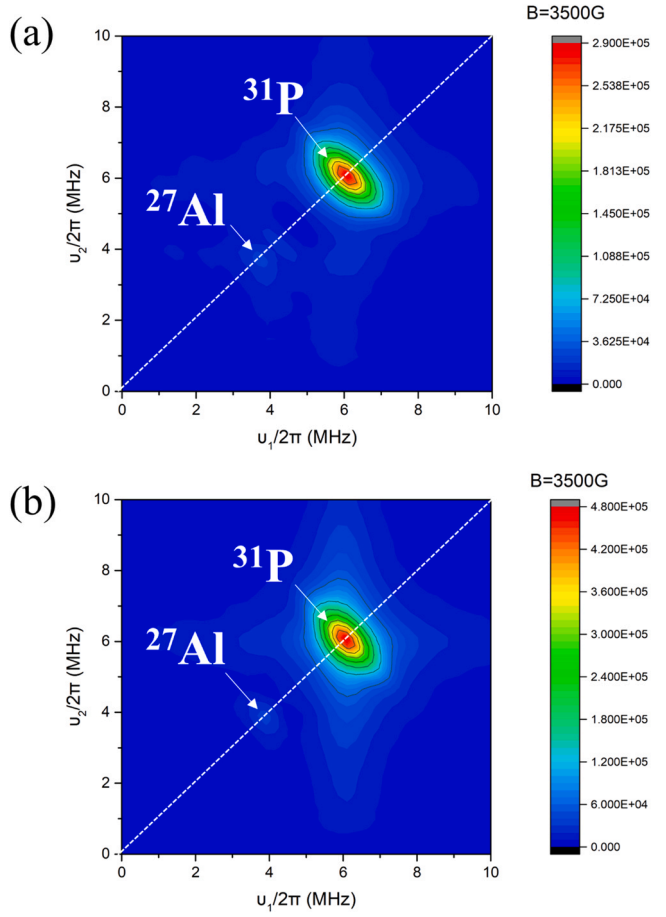

Fig. 8. HYSCORE EPR spectra of an as-melted glass (a) and its dehydroxylated sample after remelting in N_2 at 850 °C for 5 h (b).

were not detected due to their extremely low natural abundance (~ 0.038%). In addition, no magnetic nuclei ^{1}H were detected in as-melted and dehydroxylated samples using HYSCORE or 3 P-ESEEM, which implies that OH may not be located in the local coordination environment of Nd^{3+} ions (distance range 4–8 Å).

The methodology of dehydroxylation employed herein has been revealed again as a very effective way of preparing homogeneous and water free phosphate glasses, in the present case of an alumino-phosphate composition. The process has also been scaled successfully from 5 g to 50 g samples, which with the usual laboratory means can already be considered a potential way of producing small scale optical glasses for commercial and research purposes. Despite the process has to be carried out in two steps: a first melting in a ceramic crucible followed by the dehydroxylation and fining treatment in the graphite crucible under N_2 flow, the final grade of chemical and optical homogeneity allows considering the whole process as very competitive from all points of view.

The dehydroxylation reaction is directly dependent on the viscosity of the phosphate melt and, most particularly, from the diffusion coefficient of water molecules in it. Provided that one knows the viscosity of the melt, it is thus possible to calculate the water diffusion coefficient and optimize the temperature at which the dehydroxylation can be more efficient. Furthermore, the dependence of the OH absorption coefficient has been well determined as a function of the mass of glass and of the reaction time, so it may also be possible to optimize the right time necessary for any given initial mass of glass in order to reach the sufficient homogeneity all across the bulk glass sample.

The chemical composition used in this study has been chosen with respect to the one employed for our first study [5] although the main intention was now studying a glass having Al_2O_3 in view of the better thermo-mechanical properties. Actually, some of the properties measured in this study fit very well those of most relevant commercial laser phosphate glasses for high energy and power applications [1]. However, from the spectroscopic point of view as it will be seen below, the most important characteristic that made this process successful is without any doubt the fact that it can be possible the preparation of very homogeneous and water free laser glasses.

3.2. Spectroscopic and lasing properties

A last batch was melted containing a 2.5 wt% of Nd_2O_3 that was added to the nominal glass composition, being thus the Nd_2O_3 content of ca. 0.92 mol%. The 25 g of the as-melted glass were dehydroxylated at 850 °C for 10 h and the results of its main properties

Table 3
Properties of the 2.5 wt% Nd_2O_3 phosphate laser glass.

Glass transition temperature (°C)	366 ± 1
Coefficient of thermal expansion (CTE) (× 10^{-6} K^{-1}) (20–300 °C)	17.7 ± 0.2
Density (g cm^{-3})	2.8285
Molar mass (g mol^{-1})	127.64
Molar volume (cm^3 mol^{-1})	45.13
Refraction index (@ 532 nm)	1.4948 ± 0.0028
Young's modulus (GPa)	47.01 ± 0.44
Poisson's coefficient	0.2756 ± 0.0033
Vickers Hardness (GPa)	3.9 ± 0.2
OH absorption coefficient (cm^{-1}) at 3000 cm^{-1}	0.62

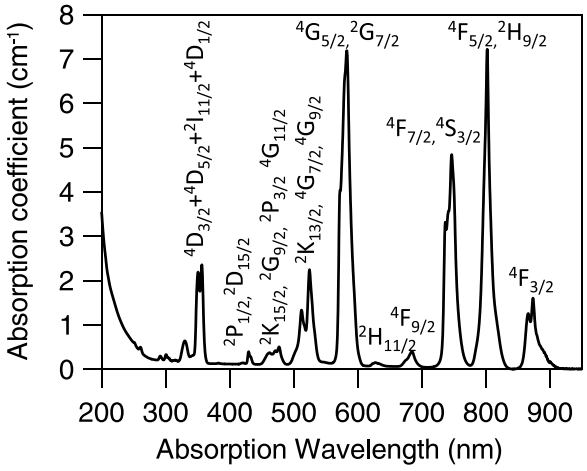

Fig. 9. Room temperature absorption spectrum of Nd^{3+} ions in the studied glass doped with 2.5 wt% Nd_2O_3.

have been gathered in Table 3, i.e. T_g and coefficient of thermal expansion, density, refractive index, Young's modulus, coefficient of Poisson, hardness, and OH absorption coefficient at 3000 cm^{-1}. This glass was then used for studying the spectroscopic and lasing properties of Nd^{3+} ions as it will be shown below.

3.2.1. Absorption and emission properties

The room temperature emission spectrum was recorded in the 200–2600 nm range. Fig. 9 shows the absorption coefficient in the 200–950 nm spectral range. The spectrum shows the bands corresponding to the transitions from the $^4I_{9/2}$ ground state to the excited states of Nd^{3+} ion. Data from this spectrum can be used to calculate the radiative properties of the emissions from the $^4F_{3/2}$ excited state according to the Judd-Ofelt theory [17,18]. The absorption bands were integrated and these data together with the values of the refractive index and Nd^{3+} concentration (2.47×10^{20} cm^{-3}) were used to calculate the Judd-Ofelt parameters (JO). The obtained values for this glass are $\Omega_2 = 4.5 \times 10^{-20}$ cm^2, $\Omega_4 = 3.5 \times 10^{-20}$ cm^2 and $\Omega_6 = 5.6 \times 10^{-20}$ cm^2, with a root-mean-squared deviation equal to 4.75×10^{-7}. These values are in the observed range for phosphate glasses [6]. The experimental and calculated oscillator strengths are displayed in Table 4. The good agreement between experimental and calculated oscillator strengths indicates the good fitting of JO parameters.

The JO parameters have been used to calculate the radiative transition probabilities, the radiative lifetime and branching ratios for the emission from the $^4F_{3/2}$ to the ^4I_J ($J = 9/2$, 11/2, 13/2, 15/2) states.

The radiative transition probability from the initial manifold $|(S, L)J>$ to the terminal manifold $|(S'L')J'>$ is given by [19]:

$$A[(S, L)J; (S'L')J'] = \frac{64\pi^4 e^2}{3h\lambda^3(2J+1)} n \frac{(n^2+2)^2}{9} \sum_{t=2,4,6} \Omega_t \left|\langle (S, L)J \| U^t \| (S', L')J' \rangle\right|^2 \quad (7)$$

where $n\frac{(n^2+2)^2}{9}$ is the local field correction for electric dipole transitions, n is the refractive index, λ is the wavelength of the transition, Ω_t are the JO parameters, and $|\langle (S, L)J \| U^t \| (S', L')J' \rangle|^2$are the doubly reduced matrix elements of the unit tensor operator of rank t = 2, 4, and 6. These matrix elements are independent of the ion environment [20]. In the case of overlapping transitions, the matrix elements of the corresponding transitions were summed.

The radiative lifetime is related to the radiative transition probability by [19]:

$$\tau_R = \left(\sum_{S,L,J} A[(S, L)J; (S'L')J'] \right)^{-1} \quad (8)$$

The branching ratio can be obtained from the transition probabilities by using [19]:

$$\beta_R = \frac{A[(S, L)J; (S'L')J']}{\sum_{S,L,J} A[(S, L)J; (S'L')J']} \quad (9)$$

The radiative transition probabilities and branching ratios together with the total radiative probability from the $^4F_{3/2}$ state are displayed in Table 5. The emission intensity of the $^4F_{3/2} \rightarrow {}^4I_{11/2}$ laser transition only depends on the Ω_4 and Ω_6 parameters and can be characterized by the spectroscopic quality factor Ω_4/Ω_6. To maximize the emission intensity of the $^4F_{3/2} \rightarrow {}^4I_{11/2}$ laser transition one requires $\Omega_4 << \Omega_6$ [21]. In this glass the spectroscopic quality factor is 0.6, in agreement with the large branching ratio for the $^4F_{3/2} \rightarrow {}^4I_{11/2}$ laser transition.

The $^4F_{3/2} \rightarrow {}^4I_{11/2,13/2}$ emission spectrum was measured at room temperature by exciting the samples at 802 nm in resonance with the $^4I_{9/2} \rightarrow {}^4F_{5/2}, {}^2H_{9/2}$ absorption band. As can be seen in Fig. 10, the emission bands are inhomogeneously broadened due to site-to-site variations in the local ligand field. The emission band for the $^4F_{3/2} \rightarrow {}^4I_{11/2}$ transition was integrated and divided by the peak intensity to yield an effective linewidth in order to estimate the stimulated emission cross-section of this transition by using [21]:

$$\sigma_p(\lambda_p) = \frac{\lambda_p^4}{8\pi c n^2 \Delta\lambda_{eff}} A\left[\left({}^4F_{3/2}\right); \left({}^4I_{11/2}\right) \right] \quad (10)$$

where λ_p is the peak fluorescence wavelength, n is the refractive index, $\Delta\lambda_{eff}$ is the effective linewidth, and $A[({}^4F_{3/2});({}^4I_{11/2})]$ is the radiative transition probability for this transition [19]. The stimulated emission cross-section is one of the most important laser glass properties since together with the quantum yield control the energy storage, gain coefficient, and extraction efficiency of the laser glass. The stimulated emission cross-section for the $^4F_{3/2} \rightarrow {}^4I_{11/2}$ transition is presented in Table 6, together with the refractive index (n), peak position (λ_p), effective fluorescence linewidth ($\Delta\lambda_{eff}$), radiative lifetime (τ_R) and experimental lifetime (τ_{exp}) measured by exciting at 802 nm. The value of the experimental lifetime corresponds to the fit to a single exponential function. The emission cross-section for several commercial Nd-phosphate laser glasses usually ranges

Table 4
Experimental and calculated oscillator strengths of Nd^{3+}in the studied glass.

Transition from the ground state $^4I_{9/2}$ to	f_{exp} (10^{-6})	f_{cal} (10^{-6})
$^4F_{3/2}$	1.90	1.83
$^4F_{5/2} + {}^2H_{9/2}$	7.24	6.8
$^4F_{7/2} + {}^4S_{3/2}$	6.93	7.48
$^4F_{9/2}$	0.49	0.57
$^2H_{11/2}$	0.13	0.16
$^4G_{5/2} + {}^2G_{7/2}$	16.58	16.65
$^2K_{13/2} + {}^4G_{7/2} + {}^4G_{9/2}$	5.79	4.94
$^2K_{15/2} + {}^2G_{9/2} + {}^2P_{3/2} + {}^4G_{11/2}$	1.59	1.12
$^2P_{1/2} + {}^2D_{15/2}$	0.35	0.43
$^4D_{3/2} + {}^4D_{5/2} + {}^2I_{11/2} + {}^4D_{1/2}$	8.33	8.64

Table 5
Radiative property parameters for the $^4F_{3/2} \rightarrow {}^4I_J$ ($J = 9/2$, 11/2, 13/2, 15/2) transitions of Nd^{3+} in the studied glass.

Transition $^4F_{3/2} \rightarrow$	A_R (s^{-1})	β_R
$^4I_{15/2}$	12	0.005
$^4I_{13/2}$	272.4	0.113
$^4I_{11/2}$	1279.2	0.532
$^4I_{9/2}$	837.6	0.349
$W_R(s^{-1})$	2401.2	

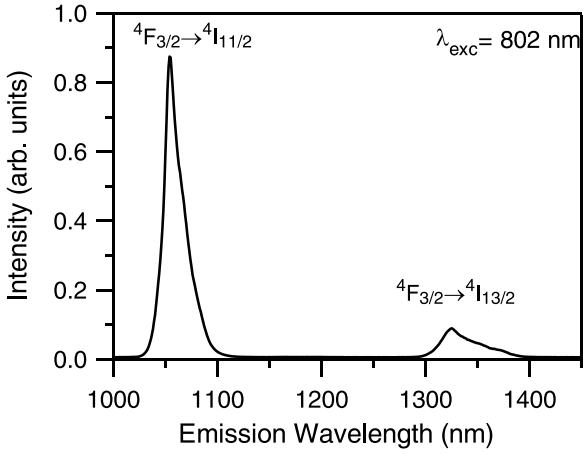

Fig. 10. Room temperature emission spectrum of the $^4F_{3/2}\rightarrow{}^4I_{11/2,13/2}$ transitions of Nd^{3+} ions in the studied glass doped with 2.5 wt% Nd_2O_3 obtained under excitation at 802 nm.

Table 6
Room temperature emission properties of Nd^{3+} in the studied glass doped with 2.5 wt % Nd_2O_3 for the $^4F_{3/2}\rightarrow{}^4I_{11/2}$ transition.

n	λ_p (nm)	$\Delta\lambda_{eff}$ (nm)	σ_p ($\times 10^{-20}$ cm^2)	τ_R (μs)	τ_{exp} (μs)
1.4948	1055	24	3.9	416	370

between 3 and 4×10^{-20} cm^2 [1]. The studied glass presents the same emission cross-section than commercial LG-770 (Schott) glass which is currently used for high power laser inertial confinement fusion (ICF) [1,6].

Another important parameter in an optical amplification process is the experimental lifetime of the $^4F_{3/2}$. The experimental decay of the $^4F_{3/2}$ state was obtained by exciting with a pulsed Ti-sapphire laser at 802 nm in the $^4I_{9/2}\rightarrow{}^4F_{5/2}$ absorption band at room temperature. As can be seen in Fig. 11, the decay is single exponential with a lifetime of 370 μs. According to the value of the radiative lifetime the quantum efficiency ($\eta=\tau_{exp}/\tau_R$) is 89%. This reduction of the quantum efficiency indicates the presence of non-radiative processes. The decay time from level $^4F_{3/2}$ should be the sum of probabilities from radiative and nonradiative decays. The nonradiative decay includes multiphonon relaxation, Nd self-quenching, and quenching produced by impurities. In this case the nonradiative decay by multiphonon relaxation is generally small because of the large energy gap between $^4F_{3/2}$ and $^4I_{15/2}$ levels (≈5500 cm^{-1}) and the

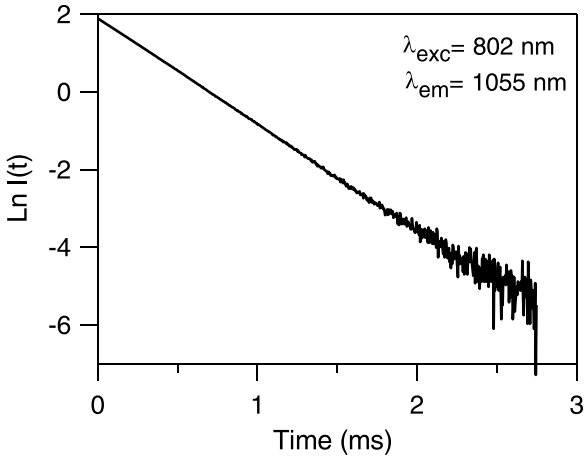

Fig. 11. Semilogarithmic plot of the experimental decay from the $^4F_{3/2}$ state. The decay was obtained by exciting at 802 nm and monitored at 1055 nm.

energy of the phonons involved (≈1100–1200 cm^{-1}) [6]. Therefore five phonons are needed to bridge the gap which indicates that multiphonon relaxation process is weak and it could be neglected. Another possible contribution to the nonradiative decay could be the effect of OH groups, however, the low value (0.62 cm^{-1}) of the OH absorption coefficient at 3000 cm^{-1} for this glass, suggests that the OH quenching effect is not very significant [22]. This value is close to the one reported in LG-770 (≤0.5) and lower than those in LHG-8 (≤ 1.5) [22] and N31 (0.85 cm^{-1}) commercial glasses [23]. Considering, the empirical relation reported in ref. 22 to estimate the decay rate due to OH quenching in phosphate glasses by using the product of the OH absorption coefficient and the quenching coefficient, the obtained value is around 40 s^{-1}. Taking into account that the total nonradiative probability is around 301 s^{-1}, we can conclude that the main quenching process should be due to Nd^{3+} self-quenching. As we have mentioned before, the lifetime is shorter than the radiative lifetime but the decay is single exponential. This behavior could be associated with rapid energy diffusion between Nd^{3+} ions. In the transfer rapid limit, the transfer takes place so quickly that transfer times are averaged out and the system shows an exponential decay as is experimentally observed [24].

The product of the stimulated emission cross-section and experimental lifetime, known as figure of merit, should be as large as possible to attain high optical gain. In this glass the value is 144.3×10^{-25} cm^2 s, which is higher than in other phosphate glasses [25]. The spectroscopic and laser parameters of this glass together with the low value of the OH absorption coefficient, close to those of commercial glass lasers such as LG-770 [6] show its suitability for laser amplification at 1055 nm as we will see in Section 3.2.3.

3.2.2. Site-selective laser spectroscopy

As it is well known, in glasses, due to the crystal field inhomogeneity at the RE sites, the $^4F_{3/2}\rightarrow{}^4I_{11/2}$ transition of Nd^{3+} ions can show variations in peak wavelength, linewidth, and spectral profile depending on pumping wavelength. This issue is of paramount importance when facing laser applications, especially, if we need a precise and stable laser emission wavelength. If crystal field inhomogeneity is present, some noticeable dependence of the output wavelength may appear as a function of the pump wavelength, when pumping with narrow spectral sources.

In order to obtain information about the crystal field site inhomogeneity of Nd^{3+} in this glass, low temperature site-selective spectroscopy by using a Ti-sapphire ring laser with a narrow bandwidth (0.4 cm^{-1}) as excitation source for the $^4I_{9/2}\rightarrow{}^4F_{3/2}$ transition has been performed. At low temperatures (4.2 K), in low symmetry sites, this transition exhibits only two Stark components. This makes easier the interpretation of the excitation spectrum of Nd^{3+}ions. As an example, Fig. 12 shows the low temperature (4.2 K) excitation spectra of the $^4I_{9/2}\rightarrow{}^4F_{3/2}$ transition obtained by collecting the luminescence at different wavelengths along the $^4F_{3/2}\rightarrow{}^4I_{11/2}$ transition. These spectra show, as expected, two main broad bands associated with the two Stark components of the $^4F_{3/2}$ doublet. However, as the emission wavelength increases from 1044 nm to 1058 nm, the low energy component of the spectra, broadens and red-shifts from 873 to 876 nm. Moreover, both stark components exhibit a noticeable structure indicating the contribution of at least two broad Nd^{3+} site distributions with different crystal field environments. This is especially apparent in the spectrum collected at the shortest wavelength (1044 nm in Fig. 12).

The site-selective steady-state emission spectra of the laser transition were obtained at 4.2 K by exciting at different wavelengths along the low energy component of the $^4F_{3/2}$ doublet. As an example, Fig. 13 shows the spectra obtained at 874, 876, 878, 880, and 882 nm. As can be seen, the shape, peak position and linewidth of the emission band change with the excitation wavelength. The excitation at the low energy side of the $^4I_{9/2}\rightarrow{}^4F_{3/2}$ leads to narrower and

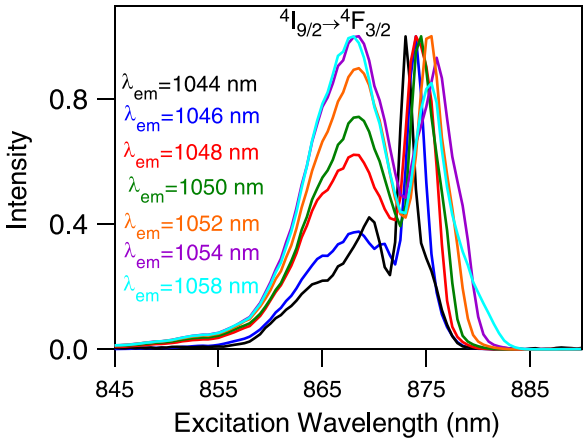

Fig. 12. Normalized excitation spectra of the $^4I_{9/2}\rightarrow{}^4F_{3/2}$ transition obtained by collecting the luminescence at different emission wavelengths along the $^4F_{3/2}\rightarrow{}^4I_{11/2}$ emission for the studied glass doped with 2.5 wt% Nd_2O_3. Data correspond to 4.2 K.

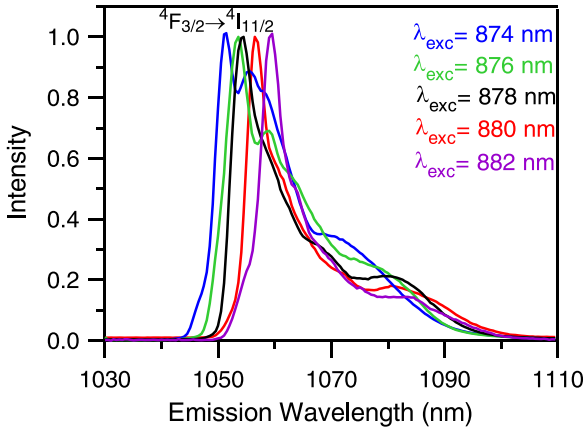

Fig. 13. Normalized steady-state emission spectra of the $^4F_{3/2}\rightarrow{}^4I_{11/2}$ transition for different excitation wavelengths along the low Stark component of the $^4F_{3/2}$ level for the studied sample doped with 2.5 wt% Nd_2O_3. Data correspond to 4.2 K.

less structured ref-shifted emission spectra. The effective linewidth is reduced from about 19–12 nm when the excitation wavelength increases from 874 to 882 nm, whereas the emission peak shifts from 1051.5 to 1059.5 nm. Similar variations in fluorescence profile, peak position, and linewidth have been observed in other phosphate glasses [26]. As a conclusion, the results displayed in Figs. 12 and 13 clearly show the crystal field inhomogeneity at the Nd^{3+} sites in this glass as well as the complexity of their distribution.

3.2.3. Laser emission

In order to investigate the properties of the laser emission of Nd^{3+} in this glass, we have pumped the $^4F_{5/2}$ level around 800 nm by using a 0.1 nm spectral and 10 ns temporal width tunable Ti:sapphire pulsed laser. The spontaneous emission obtained by pumping this level, which has a much higher emission cross section, occurs from the $^4F_{3/2}$ level which is placed about one average phonon energy below it (≈1100 cm^{-1}); therefore, we expect similar site dependence and spectral features of the emission profiles. As an example, Fig. 14 shows two emission profiles obtained at 806 and 876 nm by pumping the $^4F_{5/2}$ and $^4F_{3/2}$ levels, respectively.

Laser experiments were performed using a 5 mm thick plate-shaped sample with polished faces doped with ca. 2.5 wt% Nd_2O_3 concentration. The pump beam is concentrated to 1.2 mm diameter by means of a lens and the sample situated slightly out of the pump focus to avoid thermal damage. A 10 cm long confocal symmetrical resonator was built with two concave mirrors, one HR and an output

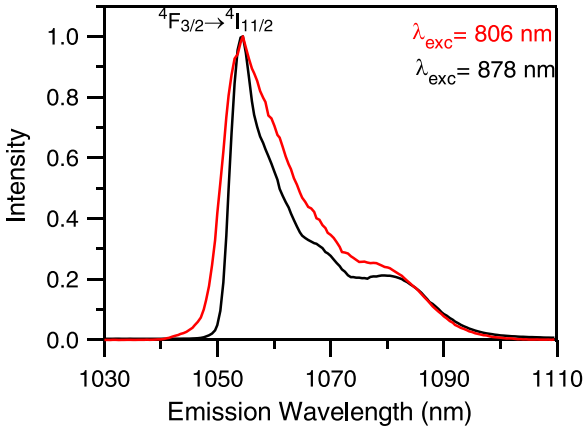

Fig. 14. Normalized steady-state emission spectra of the $^4F_{3/2}\rightarrow{}^4I_{11/2}$ transition for two different excitation wavelengths, 806 nm (red) and 878 (black). Data correspond to 4.2 K.

coupler of reflectivity 70%, in a longitudinal pumping scheme. The sample plate was placed at the center of the resonator oriented at Brewster angle with respect to the resonator axis.

Two multimode fibers capture laser radiation diffused from the sample. One of them is addressed to a fast detector SIR5 (rise time 70 ps), connected to a digital oscilloscope which allows us to observe the temporal evolution of both pumping and laser output pulses. The second one is connected to a diode-array Hamamatsu-Triax 190 spectrum analyzer using a 1200 lines/mm diffraction grating and allows us to observe the spectra of the output laser pulses, after filtering the pumping residual signal. The system setup is shown in Fig. 15.

The main laser output results are shown in Fig. 16. By pumping at the maximum of the $^4F_{5/2}$ absorption level (802 nm), the $^4F_{3/2}\rightarrow{}^4I_{11/2}$ laser emission band of Nd^{3+} ion expands over about six nm with an effective linewidth around 1.7 nm. As expected, the laser emission undergoes detectable changes when the excitation wavelength is tuned along the $^4I_{9/2}\rightarrow{}^4F_{5/2}$ pump band due to the crystal field site effects we have discussed above. It is worth noticing that tuning the pump wavelength both to the lower or higher (higher or lower energies) values, the spectrum of the laser moves from the position of the one obtained at the maximal absorption to lower energies reaching similar shapes and barycenter positions. This curious behavior can be explained if we would take into account the existence of two distributions of sites for the Nd^{3+} ions overlapped in energy;

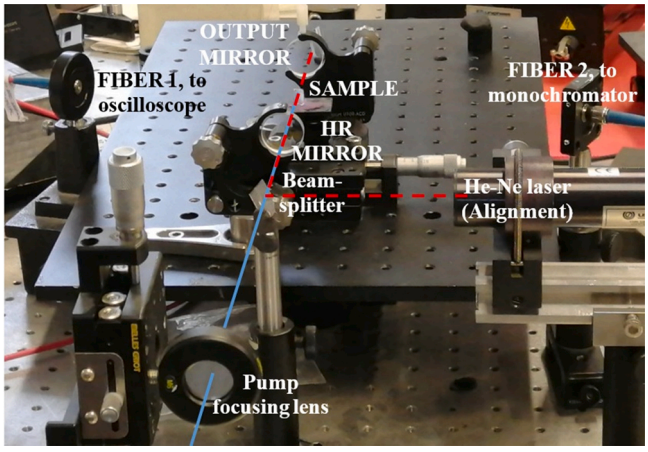

Fig. 15. Experimental set-up used for laser experiments. The sample is located at the center of a confocal resonator consisting in two concave mirrors of curvature radii 10 cm, one HR and an output coupler of reflectivity 70%. The pump beam is addressed collinear to the resonator.

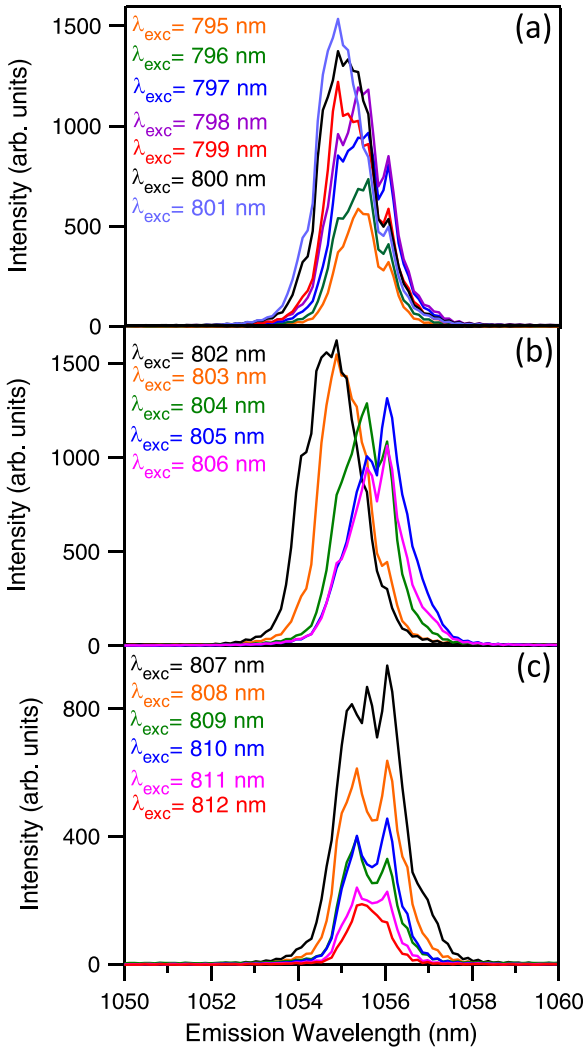

Fig. 16. Stimulated emission spectra of $^4F_{3/2} \rightarrow {}^4I_{11/2}$ transition for 2.5 wt% Nd_2O_3-doped alumino-phosphate glass obtained at different excitation wavelengths along the $^4I_{9/2} \rightarrow {}^4F_{5/2}$ absorption band.

one of them very wide but with smaller effective cross-section than the other one located close to the center of the former, whose effective-cross section is larger and sharper. This plausible argument seems to be reinforced by the experimental results shown by the excitation spectra of the $^4I_{9/2} \rightarrow {}^4F_{3/2}$ level. As we mentioned earlier, when collecting at the high-energy side of the emission band (1044 nm), a sharp excitation peak overlapping the center of the band can be observed in the high-energy Stark component.

From a practical point of view, as the laser utility we are looking for occurs close to the maximal laser output, we resume the main spectral characteristics of the device. In Fig. 16 (b) we can observe the changes in the laser emission spectrum for different pumping wavelengths between 802 and 806 nm. As can be seen, the maximum output intensity corresponds to the maximum of the $^4I_{9/2} \rightarrow {}^4F_{5/2}$ absorption. As excitation wavelength increases, the maximum of the laser output shifts from 1054.9 to 1056 nm. As mentioned before, for excitation wavelengths longer than 803 nm, the laser emission presents an additional peak at around 1055.6 nm. Moreover, the spectral effective linewidth of the laser emission changes from about 1.7–1.2 nm as the excitation wavelength increases from 802 to 812 nm.

The temporal behavior of pump and emission pulses was observed in a digital oscilloscope for 802 nm excitation wavelength. As can be seen in Fig. 17, the time-delay between pump and emission

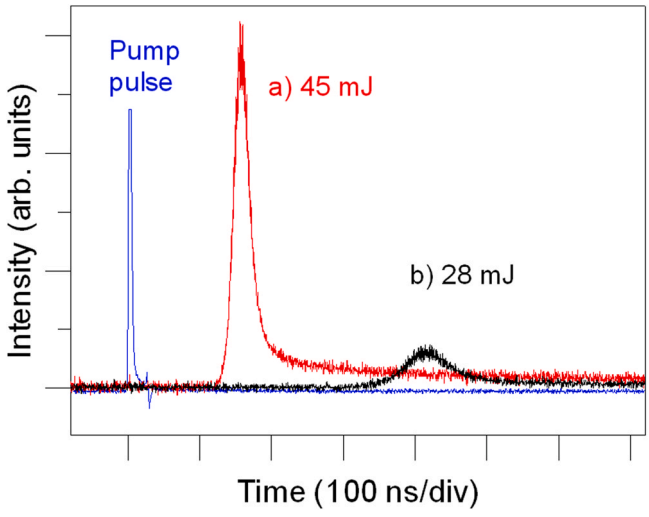

Fig. 17. Time-evolution of stimulated emission pulses in Nd^{3+}-doped alumino-phosphate glass at two different pump energies. The pump pulse (802 nm wavelength) is at left side of the graph: Black line 28 mJ pump energy, red line 45 mJ pump energy.

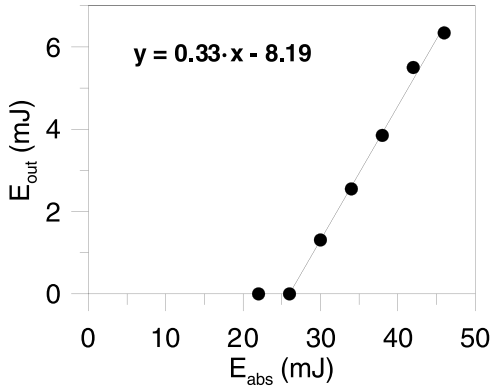

Fig. 18. Laser emission energy as a function of pump energy at 802 nm. The threshold energy is 26 mJ and the slope-efficiency is 33%.

pulses shortens as pump energy increases, as it is usual. The shortest temporal width obtained is about 25 ns with a delay respect to the pump pulse of about 150 ns.

An input/output energy graph is shown in Fig. 18. The threshold energy is 26 mJ and the slope yield in these working conditions is 33%, which could reach 40% optimizing the reflectivity of the output coupler and the coupling between the pumping beam and the emission beam.

We can evaluate the stimulated emission cross-section from threshold and optical density measurements, using the expression [26]:

$$\sigma_{em} = \frac{-logR}{0.43\, E_{th}(1 - 10^{-D})} \tag{11}$$

where E_{th} is the threshold pumping energy in photons per unit area, R is the reflectivity of the output coupler and D is the optical density of the lasing sample at pump wavelength. The result obtained is in the range $4 \pm 0.5 \times 10^{-20}$ cm^2, quite similar to the one obtained from the absorption and emission data.

4. Conclusions

The study of the processing parameters of the dehydroxylation method employed for the title glass has demonstrated that the content of water, in the form of OH ions, decreases linearly with the

remelting temperature at constant time lengths, and that it ultimately depends on the diffusion coefficient of the water throughout the melt that is ruled by the melt viscosity. The method of dehydroxylation using graphite crucibles and a- N_2 flow has shown once more to be a very effective way of dehydroxylation of this kind of phosphate glasses, which after being doped with Nd_2O_3 showed excellent optical characteristics and laser performance thanks to their very high homogeneity.

Absorption and luminescence measurements have been performed to calculate the radiative properties of the $^4F_{3/2}\rightarrow{}^4I_{11/2}$ laser transition. The stimulated emission cross-section calculated from spectral data gives a value of 3.9×10^{-20} cm^2, similar to the one of LG-770 (Shott) glass and in reasonably good agreement with the value estimated from laser threshold data ($4\pm0.5\times10^{-20}$ cm^2). The obtained values for the stimulated emission cross-section, figure of merit (144.3×10^{-25} cm^2 s), and quantum efficiency (89%) together with the threshold energy and slope-efficiency of the laser emission at around 1055 nm demonstrate the suitability of this glass for optical amplification.

The solid-state NMR results of the glass show the existence of different bonding configurations suggesting the existence of phosphate as well as mixed alumino-phosphate species. The influence of these structural features on the crystal field sensed by the rare earth, due to the presence of Al_2O_3, may explain the observed spectroscopic behavior both in the spontaneous and stimulated emissions of Nd^{3+} in this glass. In particular, the presence of P-O-Al bonds in the glass network could explain the existence of two broad sites distributions for the rare earth in the glass matrix.

CRediT authorship contribution statement

Mónica Muñoz-Quiñonero: Conceptualization, Methodology, Formal analysis, Investigation, Writing – original draft, Visualization. **Jon Azkargorta:** Methodology, Investigation, Writing – original draft, Visualization, Supervision. **Ignacio Iparraguirre:** Methodology, Investigation, Writing – original draft, Visualization, Supervision. **Rafael J. Jiménez-Riobóo:** Methodology, Formal analysis, Investigation, Writing – review & editing. **Gregory Tricot:** Methodology, Formal analysis, Investigation, Writing – original draft, Visualization. **Chongyoun Shao:** Methodology, Formal analysis, Investigation, Writing – original draft, Visualization. **Francisco Muñoz:** Conceptualization, Methodology, Formal analysis, Investigation, Writing – original draft, Writing – review & editing, Visualization, Supervision, Funding acquisition. **Joaquín Fernández:** Conceptualization, Methodology, Formal analysis, Writing – review & editing, Supervision. **Rolindes Balda:** Conceptualization, Methodology, Formal analysis, Investigation, Writing – original draft, Writing – review & editing, Visualization, Supervision, Funding acquisition.

Declaration of Competing Interest

The authors declare that they have no known competing financial interests or personal relationships that could have appeared to influence the work reported in this paper.

Acknowledgements

The authors thank funding from projects from *Agencia Estatal de Investigación* of Spain (FEDER, UE) MAT2017-87035-C2-1-P/-2-P, MAT2015-65356-C3-1-R, RTI2018-096918-B-C41, PID2020-115419GB-C21/C-22, and the project from the Basque Country Government PIBA1824.

References

[1] J.H. Campbell, J.S. Hayden, A. Marker, High power solid-state lasers: a laser glass perspective, Int. J. Appl. Glass Sci. 2 (1) (2011) 3–29.
[2] G.F. Yang, Q.Y. Zhang, S.Y. Zhao, Z.D. Deng, Z.M. Yang, Z.H. Jiang, Dehydration of Er^{3+}-doped phosphate glasses using reactive agent bubble flow method, J. Non-Cryst. Solids 352 (2006) 827–831.
[3] L.J. Cao, T.L. Yu, Q. Hong, et al., Dehydration processing in Nd^{3+}-doped phosphate laser glass, Acta Photon. Sin. 43 (2014) 1–4.
[4] Q. He, P. Wang, M. Lu, B. Peng, Investigations on the photoluminescence of the iron and cobalt doped fluoride-containing phosphate-based glasses and its defects-related nature, J. Alloy. Compd. 685 (2016) 153–158.
[5] F. Muñoz, R. Balda, A highly efficient method of dehydroxylation and fining of Nd phosphate laser glasses, Int. J. Appl. Glass Sci. 10 (2019) 157–161.
[6] J.H. Campbell, T.I. Suratwala, Nd-doped phoshpate glasses for high-energy/high-peak-power lasers, J. Non-Cryst. Solids 263&264 (2000) 318–341.
[7] R.K. Brow, R.J. Kirkpatrick, G.L. Turner, Nature of alumina in phosphate glass: II, structure of sodium aluminophosphate glass, J. Am. Ceram. Soc. 76 (76) (1993) 919–928.
[8] S. Jiang, T. Luo, M. Myers, J. Myers, J. Lucas, N. Peyghambariam, Phosphate glasses for high-average power lasers, Proc. SPIE 80 (1998) 2–13.
[9] Mahmoud M. Ismail, Inas K. Batisha, Lidia Zur, Alessandro Chiasera, Maurizio Ferrari, Anna Lukowiak, Optical properties of Nd^{3+}-doped phosphate glasses, Opt. Mater. 99 (2020) 109591.
[10] Francisco Muñoz, Akira Saitoh, Rafael Jiménez-Riobóo, Rolindes Balda, Synthesis and properties of Nd-doped oxynitride phosphate laser glasses, J. Non-Cryst. Solids 473C (2017) 125–131.
[11] G. Grimvall, E.P. Wohlfarth (Ed.), Thermophysical Properties of Materials, North-Holland, Amsterdam, 1986.
[12] A. Lesage, D. Sakellariou, S. Steuernagel, L. Emsley, Carbon–proton chemical shift correlation in solid-state NMR by through-bond multiple-quantum spectroscopy, J. Am. Chem. Soc. 120 (1998) 13194–13201.
[13] C.B. Thorsness, T.I. Suratwala, R.A. Steele, J.H. Campbell, Dehydroxylation of phosphate laser glass, Proc. SPIE 4102 (2000) 175–194.
[14] S. Wegner, L. van Wüllen, G. Tricot, The structure of aluminophosphate glasses revisited: application of modern solid state NMR strategies to determine structural motifs on intermediate length scales, J. Non-Cryst. Solids 354 (2008) 1703–1714.
[15] G. Tricot, Mixed network phosphate glasses: seeing beyond the 1D 31P MAS NMR spectra With 2D X/^{31}P NMR correlation maps, Annu. Rep. NMR Spectrosc. 96 (2019) 35–75.
[16] G. Tricot, Insertion of Al_2O_3 in zinc metaphosphate glasses: new insights from 1D/2D solid state NMR, J. Phys. Chem. C 125 (2021) 9210–9218.
[17] B.R. Judd, Optical absorption intensities of rare-earth ions, Phys. Rev. 127 (1962) 750–761.
[18] G.S. Ofelt, Intensities of crystal spectra of rare-earth ions, J. Chem. Phys. 37 (1962) 511–520.
[19] W.F. Krupke, Induced emission cross-sections in neodymium laser glasses, IEEE J. Quantum Electron. QE-10 (1974) 450–457.
[20] W.T. Carnall, P.R. Fields, K. Rajnak, Electronic energy levels in the trivalent lanthanide aquo ions. I. Pr^{3+}, Nd^{3+}, Pm^{3+}, Sm^{3+}, Dy^{3+}, Ho^{3+}, Er^{3+}, and Tm^{3+}, J. Chem. Phys. 49 (1968) 4424–4442.
[21] R.R. Jacobs, M.J. Weber, Dependence of the $^4F_{3/2}\rightarrow{}^4I_{11/2}$ induced-emission cross section for Nd^{3+} on glass composition, IEEE J. Quantum Electron. QE-10 (1976) 102–111.
[22] Liyan Zhang, Lili Hu, Shibin Jiang, Progress in Nd^{3+}, Er^{3+}, and Yb^{3+} doped laser glasses at Shanghai Institute of optics and fine mechanics, Int. J. Appl. Glass Sci. 9 (2018) 90–98.
[23] Paul R. Ehrmann, John H. Campbell, Nonradiative energy losses and radiation trapping in neodymium-doped phosphate laser glasses, J. Am. Ceram. Soc. 85 (5) (2002) 1061–1069.
[24] M.J. Weber, Luminescence decay by energy migration and transfer: observation of diffusion-limited relaxation, Phys. Rev. B 4 (1971) 2932–2939.
[25] V.B. Sreedhar, Ramachari Doddoji, K. Kiran Kumar, Vasudeva Reddy, Minnam Reddy, A study of NIR emission and associated spectroscopic properties of Nd^{3+}: P_2O_5+K_2O+Al_2O_3+ZnF_2 glasses for 1.06 μm laser applications, J. Non-Cryst. Solids 553 (2021) 120521.
[26] I. Iparraguirre, J. Azkargorta, R. Balda, K. Venkata Krishnaiah, C.K. Jayasankar, M. Al-Saleh, J. Fernández, Spontaneous and stimulated emission spectroscopy of a Nd^{3+}-doped phosphate glass under wavelength selective pumping, Opt. Express 19 (20) (2011) 19440–19453.